Supporting Information

Green fabrication of pore-modulated carbon aerogel using biological template for high-energy density supercapacitors

Yangkai Sun[a], Dan Xu*[a], Zijian He[a], Zihang Zhang[a], Liwu Fan[a], Shurong Wang*[a b]

[a] State Key Laboratory of Clean Energy Utilization, Zhejiang University, Hangzhou 310027, China.

[b] Key Laboratory of Clean Energy and Carbon Neutrality of Zhejiang Province, Zhejiang University, Hangzhou, Zhejiang 310027, China.

*Corresponding Author:

E-mail: srwang@zju.edu.cn (Shurong Wang)

danxu_joey@zju.edu.cn (Dan Xu)

This file has 26 pages, including:

Electrochemical Measurements

COMSOL Multiphysics simulations

Figures S1 to S11

Tables S1 to S8

Reference

Figures and Tables List

Fig. S1. FTIR spectrum of the chitosan-based aerogel.

Fig. S2. SEM images of (a) samples after pre-carbonization at 400 °C, (b) BAPC-700, (c) BAPC-900 and (d) AC-800.

Fig. S3. (a) N_2 adsorption/desorption isotherm and (b) PSD of BAC-800.

Fig. S4. (a-c) N1s spectrum, (d-f) O1s spectrum of BAPC-700, BAPC-900 and AC-800.

Fig. S5. Contact angle measurements for 6 M KOH aqueous electrolyte.

Fig. S6. Faradic redox reaction.

Fig. S7. Ragone plots of BAPC-800 with high mass loading with 6 M KOH electrolyte in the two-electrode system.

Fig. S8. Specific capacitance vs. floating time for BAPC-800 at 1A g^{-1}.

Fig. S9. CV curves of BAPC-800 at different scan rates in $EMIMBF_4$ ionic liquid electrolyte in the two-electrode system.

Fig. S10. Cycling performance of BAPC-800 at 10 A g^{-1} for 5000 cycles in $EMIMBF_4$ ionic liquid electrolyte in the two-electrode system.

Fig. S11. The Raman spectra of BAPC-800 electrode before and after charge/discharge cycling.

Table S1. Element contents of BAPC-X and AC-800 from XPS results.

Table S2. Relative surface content of N/O functional groups of BAPC-X and AC-800 from XPS results.

Table S3. Comparison of the specific capacitance of BAPC-800 with reported carbon electrode materials based on KOH electrolyte.

Table S4. The mass loading, thickness, density and volumetric capacitance of electrodes of all samples.

Table S5. Comparison of density and specific capacitance of BAPC-800 with previously reported carbon electrode materials.

Table S6. The slope and intercept of the fitted line calculated by Trasatti's method of all samples.

Table S7. R_s, R_{ct} and ESR of all samples.

Table S8. Porosity and effective diffusivity of component K^+ ($D_{e,i}$) of all samples.

Electrochemical Measurements

The electrochemical performance of the samples was evaluated by cyclic voltammetry (CV), galvanostatic charge/discharge (GCD) and electrochemical impedance spectroscopy (EIS) using the PGSTAT302N Electrochemistry Station (Autolab Electrochemistry Station, Metrohm Switzerland), while the LANHE CT3001A electrochemical test system (Wuhan Rand Electronic Technology Co., Ltd., China) was employed for cyclic experiments. In the three-electrode system, the prepared single electrode was utilized as the working electrode, while the platinum sheet and Hg/HgO were employed as the counter electrode and reference electrode, respectively. The gravimetric capacitance (C_g, F g^{-1}) in the three-electrode system and the two-electrode system were calculated using the following equations, respectively:

$$C_g = \frac{I \triangle t}{m(V - IR_{drop})} \quad (1)$$

$$C_g = \frac{2I \triangle t}{m(V - IR_{drop})} \quad (2)$$

Where I (A) is the constant discharge current, Δt (s) is the discharge time, m (g) is the mass of the active material of a single electrode, V (V) is the highest voltage during discharge, and IR_{drop} is the voltage drop at the beginning of discharge.

The volumetric capacitance (C_v, F cm^{-3}) was calculated by the following equation [1, 2]:

$$C_v = \rho C_g \quad (3)$$

$$\rho = \frac{1}{V_{total} + \frac{1}{\rho_{carbon}}} \quad (4)$$

where ρ (g cm^{-3}) is the density of electrode materials, V_{total} (cm^3 g^{-1}) is the total pore volume of active material measured by N_2 adsorption-desorption isotherm, and ρ_{carbon} is the true density of carbon (2 g cm^{-3}).

The specific energy density (E, W h kg^{-1}) and power density (P, W kg^{-1}) calculated based on the two-electrode system were calculated using the following formulas:

$$E = \frac{CV^2 \times 1000}{2 \times 4 \times 3600} \quad (5)$$

$$P = \frac{E \times 3600}{\triangle t} \tag{6}$$

Where C (F g^{-1}) is the specific capacitance calculated based on the GCD curve of the two-electrode system, V (V) is the voltage window, and Δt (s) is the discharge time. The EIS test was conducted at a frequency range of 0.01 *Hz* to 100 k*Hz* with an amplitude of 5 mV, and the imaginary capacitance (C'') based on the EIS measurement was calculated using the following formula to evaluate the response speed:

$$C'' = \frac{Z'(f)}{2\pi f m |Z(f)|^2} \tag{7}$$

Where $Z'(f)$ is the real impedance, f (Hz) is the frequency, and m (g) is the mass of the active material. The relaxation time was calculated by the following formula:

$$\tau = \frac{1}{f_0} \tag{8}$$

Where f_0 (Hz) is the frequency when C" reaches the maximum value.

Floating test: symmetric supercapacitors were charged to 1.2 V and maintained for 10 h, followed by conducting three consecutive GCD cycles from 0–1.2 V at 1 A g^{-1}. The average specific capacitance was calculated based on the GCD curves. This process was repeated ten times, resulting in a total floating duration of 100 h.

Trasatti's Method Analysis

The Trasatti's method was employed to analyze EDLC and pseudocapacitance, with the following specific formula [3, 4]:

$$C = \frac{\int IdV}{m \times v \times V} \tag{9}$$

$$C^{-1} = Constant_1 \, v^{1/2} + {C_M}^{-1} \tag{10}$$

$$C = Constant_1 \, v^{-1/2} + C_E \tag{11}$$

$$C_M = C_E + C_P \tag{12}$$

$$C_E\% = \frac{C_E}{C_M} \times 100\% \tag{13}$$

$$C_P\% = \frac{C_P}{C_M} \times 100\% \tag{14}$$

Where C (F g^{-1}) represents the specific capacitance obtained by analyzing the CV curve at various scan rates, I (A) indicates the current, m (g) denotes the mass of the

active material in the electrode, v (V s^{-1}) represents the scan rate, and V (V) represents the voltage window. Assuming the ions undergo semi-infinite diffusion, plotting the reciprocal square root of specific capacitance (C^{-1}) against the square root of scan rate ($v^{1/2}$)) results in a linear relationship. The intercept of the fitted line represents the reciprocal of the total capacitance (C_M). Additionally, the specific capacitance (C) exhibits a linear relationship with the reciprocal square root of the scan rate ($v^{-1/2}$). The intercept of the fitted line represents the EDLC (C_E). Subtraction of C_E from C_M yields the maximum pseudocapacitance (C_P).

COMSOL Multiphysics simulations

In order to simulate the electrolyte transport under different pore structures during the charging process, the simulation was carried out through the "Transport of diluted species" module in COMSOL Multiphysics. A sphere with a radius of 10 μm was employed as a porous model, the boundary condition was set to 6 mol L^{-1} K^{+}, and the equation was as follows:

$$\frac{\partial c_i}{\partial t} + \nabla \cdot J_i + u \cdot \nabla c_i = 0 \tag{15}$$

$$J_i = -D_{e,i} \nabla c_i \tag{16}$$

Where J_i is the component diffusion flux, $D_{e,i}$ is the effective diffusion coefficient, and C_i is the concentration. $D_{e,i}$ were calculated by random pore model [5, 6]:

$$D_{e,i} = \varepsilon_{meso}^{2} D_{meso,i} + \frac{1 + 3 \times \varepsilon_{meso}}{1 - \varepsilon_{meso}} \varepsilon_{micro}^{2} D_{micro,i} \tag{17}$$

where ε_{micro} and ε_{meso} are the micropore and mesopore porosity of the bidisperse pore network, respectively. $D_{micro,i}$ and $D_{meso,i}$ are the transmission fluxes of micropores and mesopores, respectively, which are $1*10^{-9}$ m^2 s^{-1}. ε_{micro} and ε_{meso} can be obtained by the following formula:

$$\varepsilon_{micro} = \frac{V_{micro}}{V_{micro} + V_{meso} + V_{solid}} \tag{18}$$

$$\varepsilon_{meso} = \frac{V_{meso}}{V_{micro} + V_{meso} + V_{solid}} \tag{19}$$

Where V_{micro}, V_{meso} and V_{solid} are micropore volume, mesopore volume and solid volume, respectively. The specific data is provided by BET results.

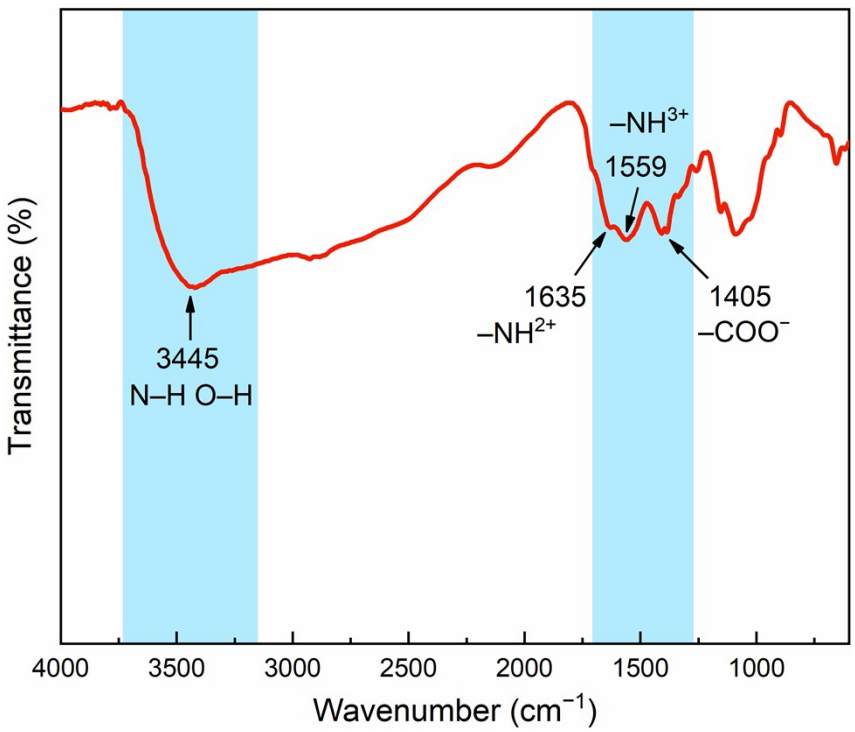

Fig. S1. FTIR spectrum of the chitosan-based aerogel.

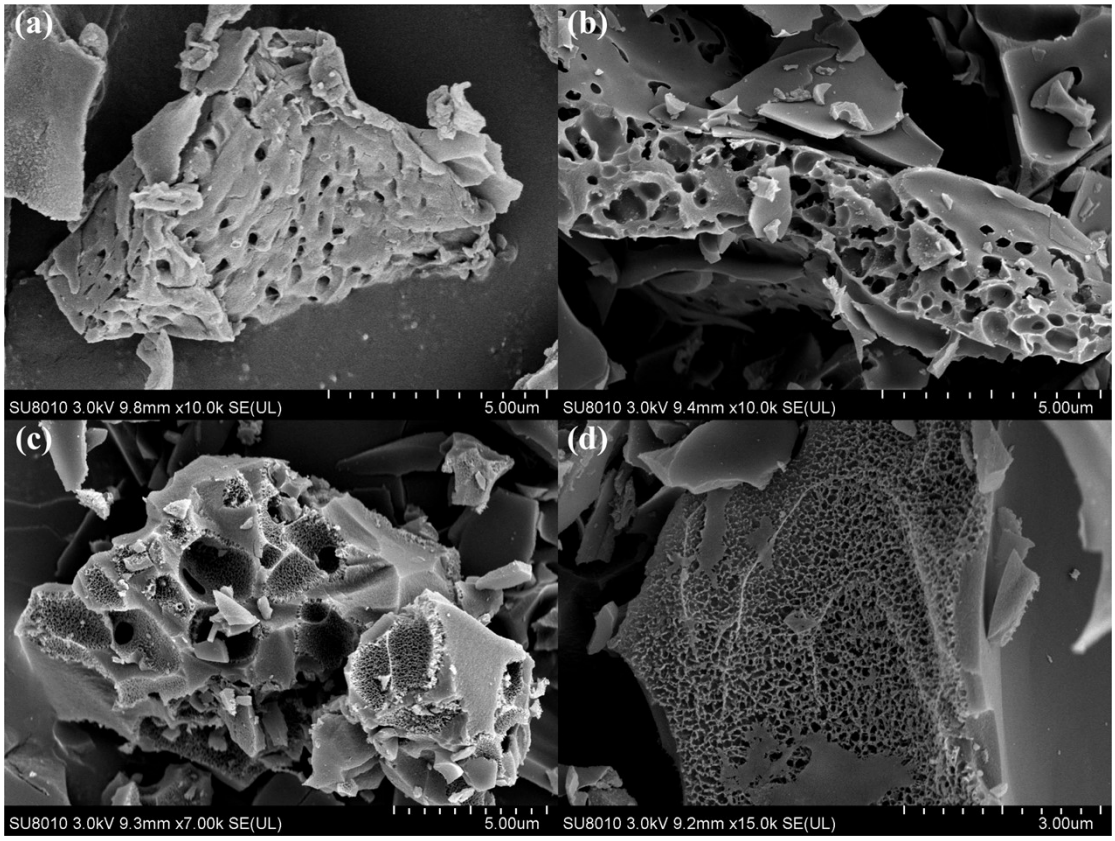

Fig. S2. SEM images of (a) samples after pre-carbonization at 400 °C, (b) BAPC-700, (c) BAPC-900 and (d) AC-800.

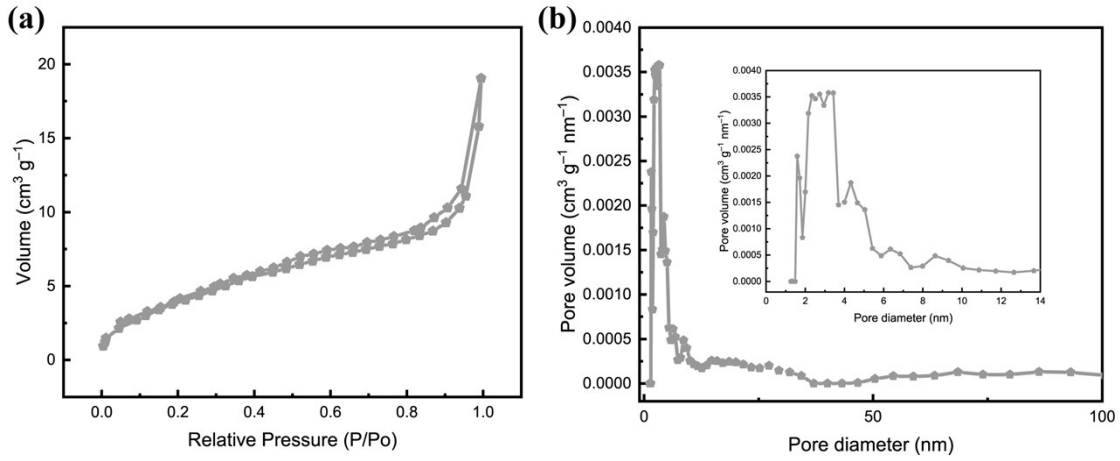

Fig. S3. (a) N_2 adsorption/desorption isotherm and (b) PSD of BAC-800.

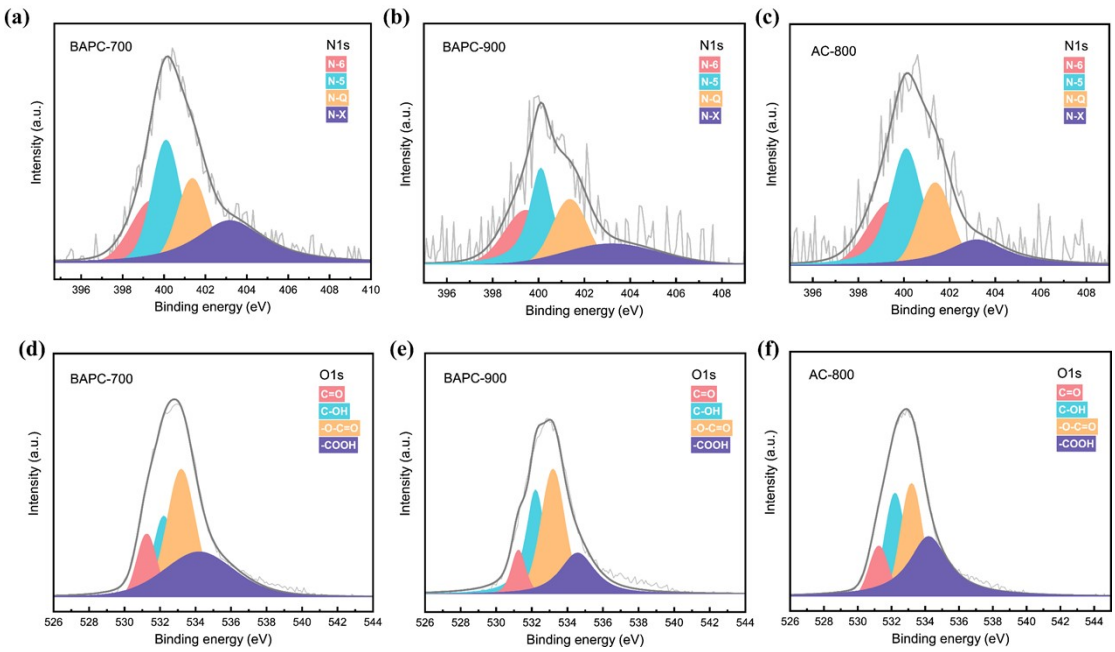

Fig. S4. (a-c) N1s spectrum, (d-f) O1s spectrum of BAPC-700, BAPC-900 and AC-800.

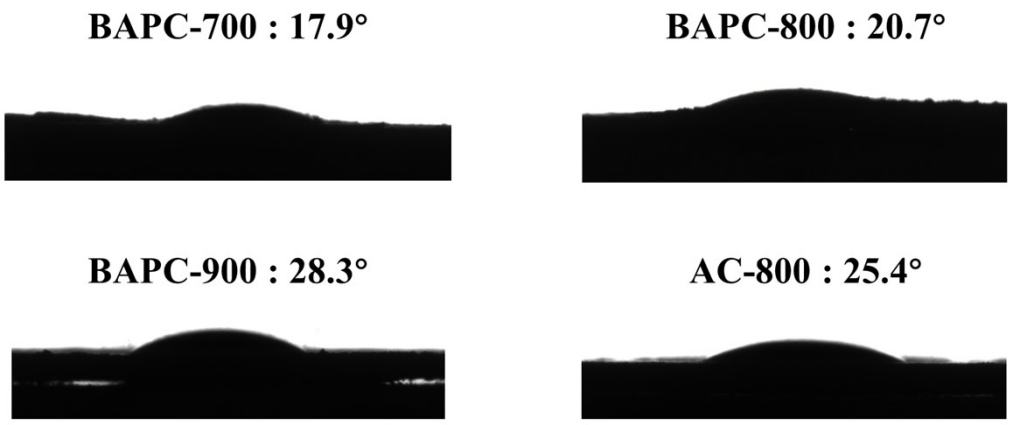

Fig. S5. Contact angle measurements for 6 M KOH aqueous electrolyte.

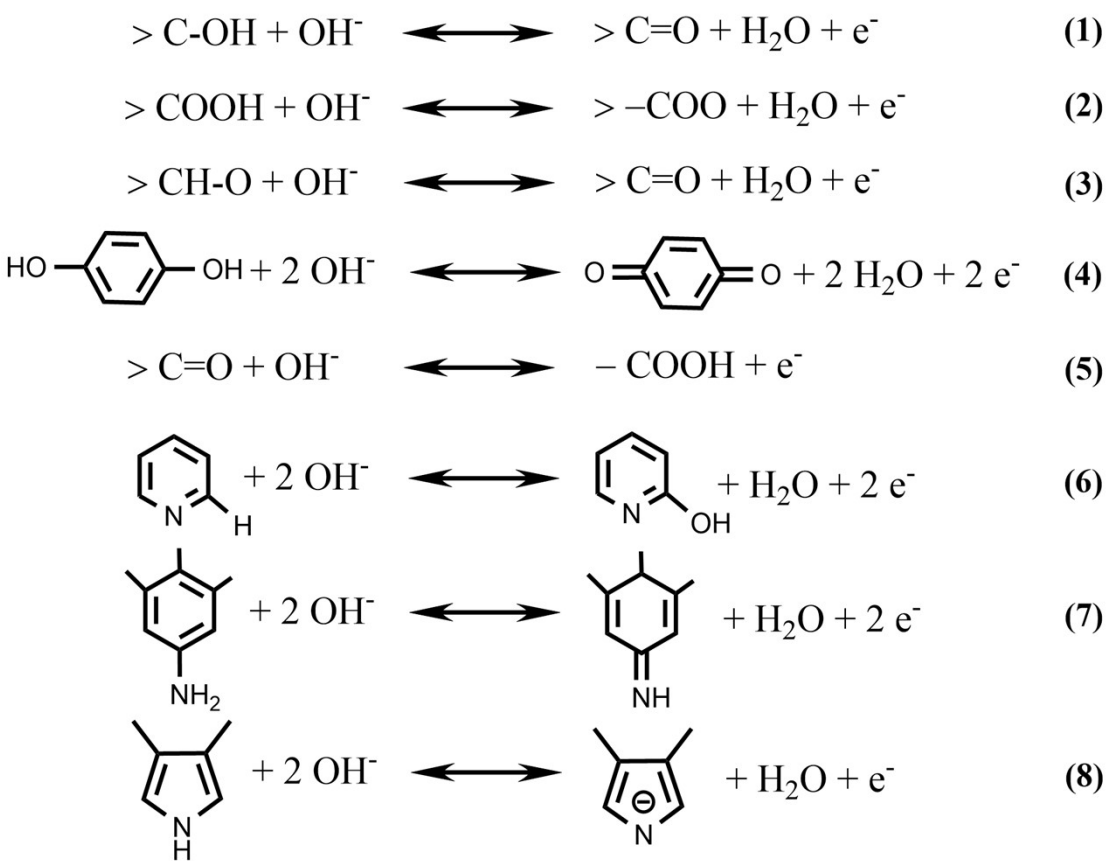

Fig. S6. Faradic redox reaction.

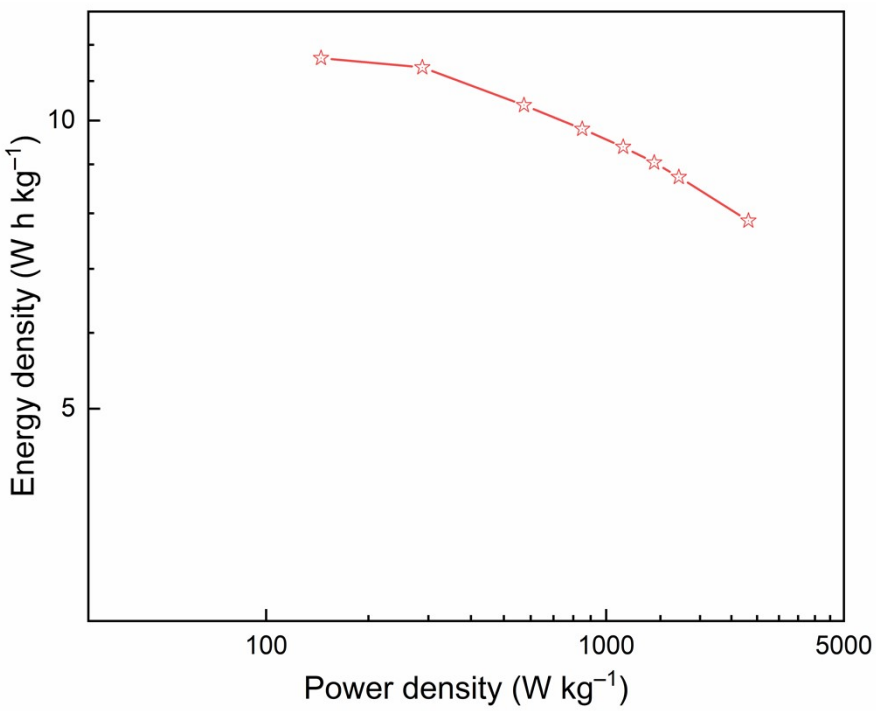

Fig. S7. Ragone plots of BAPC-800 with high mass loading with 6 M KOH electrolyte in the two-electrode system.

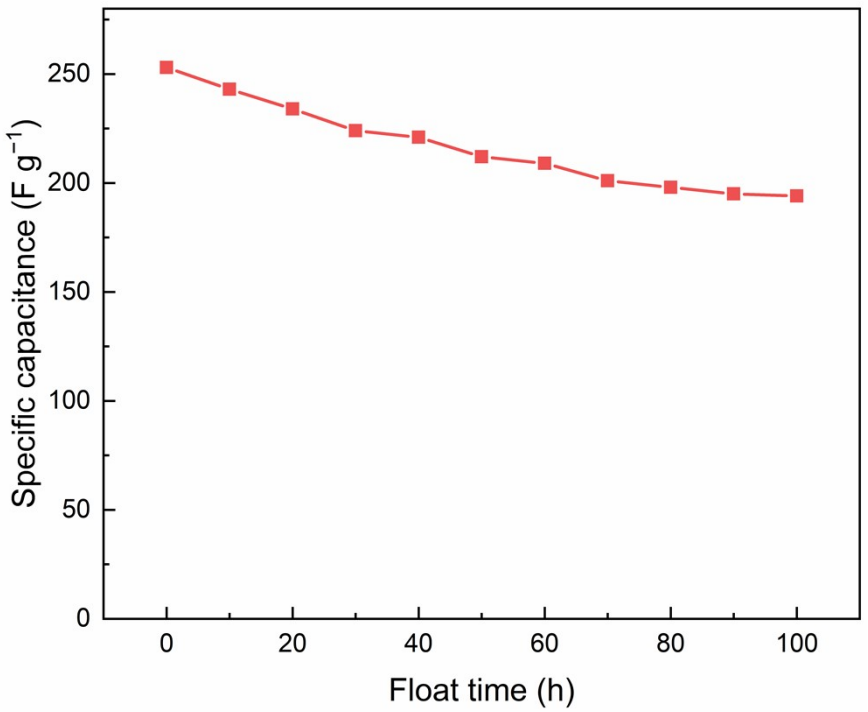

Fig. S8. Specific capacitance vs. floating time for BAPC-800 at 1A g^{-1}.

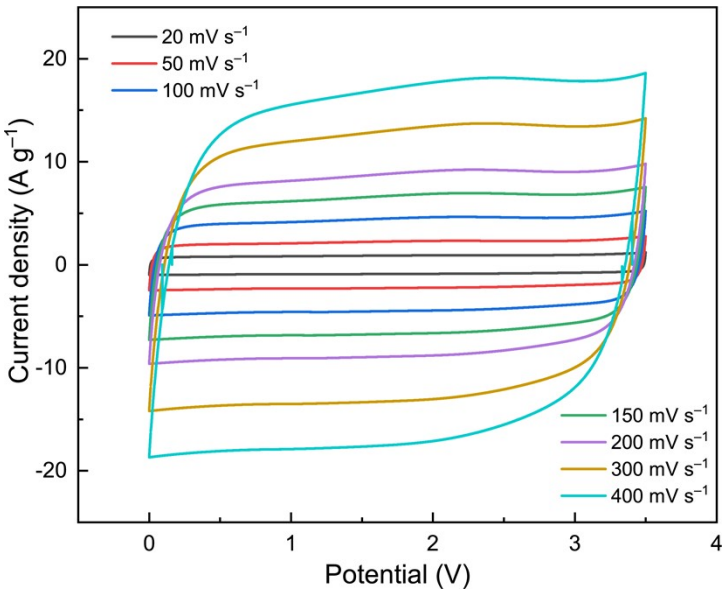

Fig. S9. CV curves of BAPC-800 at different scan rates in EMIMBF$_4$ ionic liquid electrolyte in the two-electrode system.

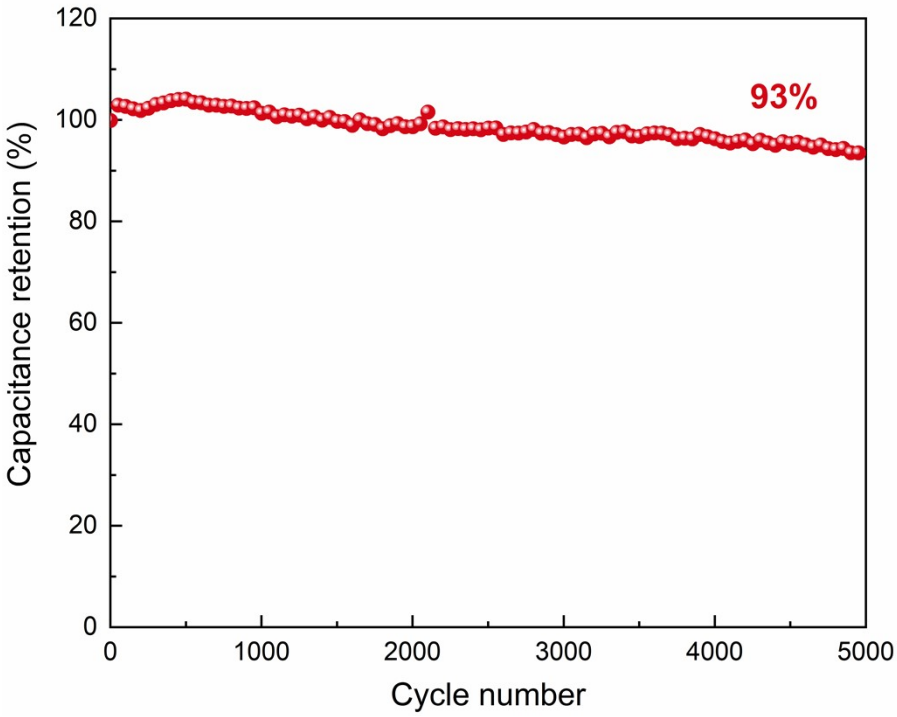

Fig. S10. Cycling performance of BAPC-800 at 10 A g^{-1} for 5000 cycles in $EMIMBF_4$ ionic liquid electrolyte in the two-electrode system.

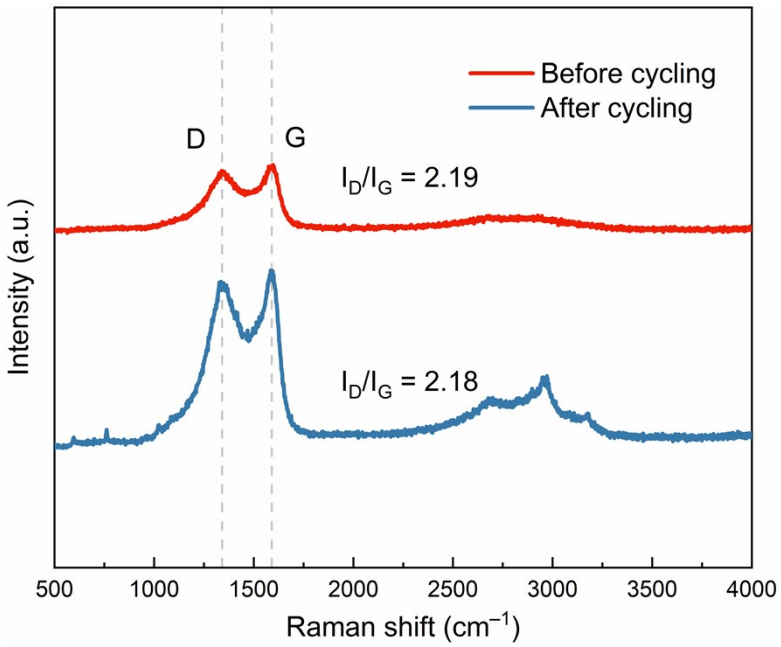

Fig. S11. The Raman spectra of BAPC-800 electrode before and after charge/discharge cycling.

Table S1. Element contents of BAPC-X and AC-800 from XPS results.

Sample	C (at. %)	N (at. %)	O (at. %)
BAPC-700	87.23	2.54	10.23
BAPC-800	88.71	1.2	10.09
BAPC-900	91.93	1.12	6.95
AC-800	89.11	1.48	9.41

Table S2. Relative surface content of N/O functional groups of BAPC-X and AC-800 from XPS results.

Sample	% of total N1s				% of total O1s			
	N-6	N-5	N-Q	N-X	C=O	C-OH	-O-C=O	-COOH
BAPC-700	21.15	29.75	21.15	27.94	11.76	18.07	37.36	32.81
BAPC-800	24.50	28.67	23.20	23.64	9.35	31.36	29.63	29.66
BAPC-900	25.18	27.37	24.30	23.15	8.69	31.45	38.04	21.82
AC-800	24.35	37.27	21.81	16.57	10.87	25.75	27.30	36.08

Table S3. Comparison of the specific capacitance of BAPC-800 with reported carbon electrode materials based on KOH electrolyte.

Materials	Electrolyte	Specific capacitance ($F\ g^{-1}$)	Reference
chitosan / acetic acid	6 M KOH	197 (0.2 A g^{-1})	7
chitosan / acetic acid / $ZnCl_2$	Aq. KOH	287.94 (1 A g^{-1})	8
chitosan / acetic acid / $ZnCl_2$	6 M KOH	267 (1 A g^{-1})	9
bio-oil / CS template / KOH	6 M KOH	351 (0.5 A g^{-1})	10
wood tar / CS template / KOH	6 M KOH	338.5 (1 A g^{-1})	11
DAB-DBQ / $CuCl_2$	6 M KOH	271 (0.5 A g^{-1})	12
chitosan / sodium lignosulfonate / H_3BO_3	6 M KOH	332 (1 A g^{-1})	13
melamine / KOH	6 M KOH	273 (0.5 A g^{-1})	14
kraft lignin	6 M KOH	244.5 (0.2 A g^{-1})	15
chitosan / acetic acid / MMS template / KOH	6 M KOH	401 (0.5 A g^{-1})	This work

Table S4. The mass loading, thickness, density and volumetric capacitance of electrodes of all samples.

Sample	Mass loading (g cm^{-2})	Thickness of electrode (mm)	ρ (g cm^{-3})	C_v (F cm^{-3})
BAPC-700	0.00136	0.0059	0.55	146
BAPC-800	0.00224	0.0052	0.43	171
BAPC-900	0.00112	0.004	0.35	99
AC-800	0.00232	0.0051	0.45	79

Mass loading: the mass loading of the active material of electrode in the three-electrode system.

Table S5. Comparison of density and specific capacitance of BAPC-800 with previously reported carbon electrode materials.

Carbon morphology	Current density ($A\ g^{-1}$)	ρ ($g\ cm^{-3}$)	C_g ($F\ g^{-1}$)	C_v ($F\ cm^{-3}$)	Reference
Porous carbon nanosheets	0.5	0.35	300	105	[16]
Hierarchical porous carbon aerogels	1	0.63	228	80	[7]
Porous bulk	0.2	0.32	540	173	[17]
Porous carbon nanosheets	0.5	0.42	267	113	[18]
Hollow nanospheres	1	0.49	180	87	[19]
Porous carbon aerogel	0.5	0.43	401	171	This work

C_V: The volumetric capacitances were calculated based on the theoretic densities of the electrode materials if the references did not give the volumetric capacitances.

Table S6. The slope and intercept of the fitted line calculated by Trasatti's method of all samples.

Sample	Constant$_1$	C_M^{-1}	Constant$_2$	C_E
BAPC-700	7.55×10^{-5}	0.00236	176.61	320.52
BAPC-800	2.60×10^{-5}	0.00208	109.08	423.55
BAPC-900	5.25×10^{-5}	0.00217	151.95	371.42
AC-800	4.32×10^{-5}	0.00364	62.43	242.95
BAC-800	3.48×10^{-4}	0.00564	114.24	107.17

Table S7. R_s, R_{ct} and ESR of all samples.

Sample	R_s (Ω)	R_{ct} (Ω)	ESR (Ω)
BAPC-700	0.29	0.21	0.018
BAPC-800	0.46	0.17	0.008
BAPC-900	0.65	0.12	0.007
AC-800	0.40	0.96	0.014
BAC-800	-	-	0.034

R_s: The solution resistance.

R_{ct}: Charge transfer resistance.

ESR: Equivalent series resistance.

Table S8. Porosity and effective diffusivity of component K^+ ($D_{e,i}$) of all samples.

Sample	ε_{micro}	ε_{meso}	$D_{e,i}$ (m^2 s^{-1})
AC-800	0.38	0.26	4.257×10^{-10}
BAPC-800	0.37	0.38	6.115×10^{-10}
BAC-800	0.0039	0.032	1.024×10^{-12}

Reference

1. C. Chen, M. Zhao, Y. Cai, G. Zhao, Y. Xie, L. Zhang, G. Zhu and L. Pan, Carbon, 2021, 179, 458-468.
2. M. Liu, J. Niu, Z. Zhang, M. Dou and F. Wang, Nano Energy, 2018, 51, 366-372.
3. K. Li, P. Li, Z. Sun, J. Shi, M. Huang, J. Chen, S. Liu, Z. Shi and H. Wang, Green Energy & Environment, 2022, DOI: https://doi.org/10.1016/j.gee.2022.01.002.
4. Y. Chang, H. Shi, X. Yan, G. Zhang and L. Chen, Carbon, 2020, 170, 127-136.
5. X. Fan, W. Zhang, Y. Xu, J. Zheng, Y. Li, X. Fan, F. Zhang, J. Ji and W. Peng, Journal of Colloid and Interface Science, 2022, 624, 51-59.
6. X. Liu, B. Qin, Q. Zhang, G. Ye, X. Zhou and W. Yuan, AIChE Journal, 2021, 67, e17163.
7. P. Hao, Z. Zhao, Y. Leng, J. Tian, Y. Sang, R. I. Boughton, C. P. Wong, H. Liu and B. Yang, Nano Energy, 2015, 15, 9-23.
8. X.-L. Zhang, C.-N. Feng, H.-P. Li and X.-C. Zheng, Cellulose, 2021, 28, 437-451.
9. Y. Gao, S. Zheng, H. Fu, J. Ma, X. Xu, L. Guan, H. Wu and Z.-S. Wu, Carbon, 2020, 168, 701-709.
10. Z. Luo, N. Lin, M. Sun, Y. Wang and X. Zhu, Carbon, 2021, 173, 910-917.
11. J. wu, M. Xia, X. Zhang, Y. Chen, F. Sun, X. Wang, H. Yang and H. Chen, Journal of Power Sources, 2020, 455, 227982.
12. L. Zheng, B. Tang, X. Dai, T. Xing, Y. Ouyang, Y. Wang, B. Chang, H. Shu and X. Wang, Chemical Engineering Journal, 2020, 399, 125671.
13. Y. Sun, D. Xu and S. Wang, Carbon, 2022, 199, 258-267.
14. X. Jing, L. Wang, K. Qu, R. Li, W. Kang, H. Li and S. Xiong, ACS Applied Energy Materials, 2021, 4, 6768-6776.
15. F. Liu, Z. Wang, H. Zhang, L. Jin, X. Chu, B. Gu, H. Huang and W. Yang, Carbon, 2019, 149, 105-116.
16. X. Fan, C. Yu, J. Yang, Z. Ling, C. Hu, M. Zhang and J. Qiu, Advanced Energy Materials, 2015, 5, 1401761.
17. J. Pokrzywinski, J. K. Keum, R. E. Ruther, E. C. Self, M. Chi, H. Meyer Iii, K. C. Littrell, D. Aulakh, S. Marble, J. Ding, M. Wriedt, J. Nanda and D. Mitlin, Journal of Materials Chemistry A, 2017, 5, 13511-13525.
18. X. Zheng, W. Lv, Y. Tao, J. Shao, C. Zhang, D. Liu, J. Luo, D.-W. Wang and Q.-H. Yang, Chemistry of Materials, 2014, 26, 6896-6903.
19. S.-Z. Zeng, Y. Yao, L. Huang, H. Wu, B. Peng, Q. Zhang, X. Li, L. Yu, S. Liu, W. Tu, T. Lan, X. Zeng and J. Zou, Chemistry – A European Journal, 2018, 24, 1988-1997.